Exploring the impact of surface oxygen vacancies on charge carrier dynamics in BiVO$_4$ photoanodes through atmospheric pressure plasma jet post-treatment for efficiency improvement in photoelectrochemical water oxidation

Kai-An Tsai [a,1], Chien-Chih Lai [a,1], Yu-Hung Chen [b], Ing-Chi Leu [a], Jui-Cheng Chang [c], Che-Yu Kuo [a], Shih-Wen Tseng [d], Yan Li [e], Ying-Chih Pu [a,*]

[a] Department of Materials Science, National University of Tainan, Tainan 700301, Taiwan
[b] School of Medicine, College of Medicine, National Cheng Kung University, Tainan 70101, Taiwan
[c] Department of Chemical Engineering and R&D Center for Membrane Technology, Chung Yuan Christian University, Taoyuan 320314, Taiwan
[d] Core Facility Center of National Cheng Kung University, Tainan 70101, Taiwan
[e] School of Materials Science and Engineering, University of Science and Technology Beijing, Beijing 100083, China

ARTICLE INFO

ABSTRACT

We have demonstrated the production of high-density surface oxygen vacancy (ov$_s$) in BiVO$_4$ (BVO) photoanodes through the post-treatment of an atmospheric pressure plasma jet (APPJ). The 3.4-fold enhancement of photo-current density of BVO photoanodes at 1.23 V$_{RHE}$ for photoelectrochemical (PEC) water oxidation due to 95 % of charge transfer efficiency at the BVO/electrolyte interface. In-situ transient absorption spectroscopy investigations provided insights into the charge carrier dynamics of the APPJ-treated BVO photoanode, revealing that abundant electrons could effectively be trapped in the ov$_s$ states to prevent charge carrier recombination. NiOOH/FeOOH oxygen evolution co-catalyst was further decorated on the APPJ-treated BVO photoanode resulted in a remarkable photocurrent density of 3.6 mA/cm^2 at 1.23 V$_{RHE}$, an anodic bias photon-to-current efficiency of 1.4 % at 0.62 V$_{RHE}$, and a faradaic efficiency over 90 % in PEC water splitting. Our study provides important and novel insights into the surface vacancy engineering of metal oxides for green hydrogen production.

1. Introduction

The development of green hydrogen (H$_2$), a clean fuel produced through water splitting using renewable sources, has emerged as a crucial objective in the global endeavor to achieve a net-zero carbon emission [1,2]. Among the various technologies for green H$_2$ production, photoelectrochemical (PEC) water splitting represents a promising approach to generate environmentally friendly H$_2$ utilizing solar energy with low applied bias [3,4]. In this system, p-type and n-type semiconductors function as photocathodes and photoanodes, respectively, to facilitate the H$_2$ and oxygen (O$_2$) evolutions via water splitting [5]. The inherent characteristics of semiconductor photoelectrodes, such as their electronic band structure, bandgap (E$_g$) and chemical stability, profoundly impact the performance of water splitting in PEC system [6].

However, it is worth noting that the theoretical efficiency of photocathodes surpasses that of photoanodes, resulting in a significant performance gap between the two, thereby limiting the efficiency of PEC water splitting [7]. One of the key challenges lies in the fact that photoanodes, mainly comprised of metal oxides such as TiO$_2$, ZnO, and WO$_3$, are characterized by large Eg values, restricting photon absorption to the UV region [8,9]. Consequently, the development of exceptional photoanodes with reduced E$_g$ becomes crucial to enhance the capture of photons across a broader range of sunlight, thereby playing a pivotal role in achieving high solar-to-hydrogen efficiency in PEC water splitting.

Bismuth vanadate (BiVO$_4$, BVO) has emerged as a promising photoanode candidate for PEC water oxidation due to its appropriate E$_g$ for visible light absorption and suitable valence band (VB) potential [10].

However, the performance of BVO photoanodes is significantly limited by poor charge carrier mobility and low charge transfer efficiency at the BVO/electrolyte interface, preventing their efficiency from the theoretical maximum in PEC water oxidation [11]. To overcome these challenges, various strategies have been explored to enhance the intrinsic properties of BVO photoanodes, including heterojunction development [12,13], crystal face engineering [14,15], elemental doping [16,17], and vacancy defect engineering [18,19]. Among these strategies, the introduction of oxygen vacancy (ov) into BVO photoanodes using different methods has shown promise in improving efficiency in the PEC water oxidation [10]. The generation of bulk ov (ov_b) in BVO photoanodes not only tunes the electronic structure to enhance charge carrier density, but also promotes their charge separation, leading to improved hole injection from BVO to electrolyte during the PEC water oxidation [19,20]. For instance, black BVO photoanodes with ov_b obtained through H_2 plasma treatment have demonstrated a smaller Eg for better solar energy utilization, as well as enhanced charge transport and separation, resulting in remarkable efficiency in PEC water splitting [21]. In a study by Wang et al., in situ formation of ov_b in BVO was achieved by incorporating a sulfur oxidation process during the preparation of BVO photoanodes [22]. When decorated with NiFeOx as the oxygen evolution co-catalyst (OEC), these BVO photoanodes exhibited a charge separation efficiency of ~98 % and a photocurrent density of 6.24 mA/cm^2 at 1.23 V_{RHE}. Furthermore, BVO photoanodes with abundant ov_b can be fabricated by thermally treating the bismuth precursor film with vanadyl acetylacetonate vapors [23]. The presence of enriched ov_b prevents bulk recombination of charge carrier, thereby promoting the photoactivity of BVO photoanodes in the PEC water oxidation. Although the presence of ov_b in BVO photoanode holds potential benefit in enhancing their photoactivity in the PEC water oxidation, suitable and simple methods to avoid the formation of negative defects that serve as charge recombination centers are still needed.

Recently, attention has been given to post-treatments to generate surface ov (ov_s) in BVO photoanodes [24–26]. The presence of ov_s serves as adsorption sites for the formation of oxy/hydroxy-based water oxidation intermediates, increasing the surface photoreaction kinetics of the PEC water oxidation [10]. Density functional theory calculations have suggested that the adsorption energies of H_2O_{ads}, OH_{ads}, and O_{ads} on BVO with ov_s are higher than those on pristine BVO, indicating the improved hole transfer efficiency at BVO/electrolyte interface during PEC water oxidation [27]. Experimental results have also demonstrated the advantages of ov_s in BVO photoanode for PEC applications. Ionized argon plasma technology has been introduced to generate ov_s in nanoporous BVO photoanodes, resulting in a ~2.3-fold improvement in the efficiency of PEC water splitting [28]. Additionally, the post-synthetic chemical reduction approach has been reported to create ov_s in BVO photoanodes, resulting in a 1.7-fold enhancement of photoactivity in PEC water oxidation compared to pristine BVO [29]. However, despite these proposed post-treatments to produce ov_s in BVO photoanode, a more convenient strategy is required to effectively control the density of ov_s. Moreover, understanding of the effects of ov_s on charge carrier dynamics at the interface between BVO and the electrolyte during PEC water oxidation remains incomplete.

Transient absorption spectroscopy (TAS) combined with photocatalytic reaction systems has proven to be a powerful tool to understanding the interplay between charge carrier recombination and chemical reactions in semiconductors during photocatalysis [30–32]. For example, Chen et al. utilized TAS in conjunction with photocatalytic reactor to study the charge carrier dynamics of $CsPbBr_3$/g-C_3N_4 nanoheterostructures (NHSs) during photocatalytic CO_2 reduction [33]. They found that the half-life time of photoexcited electrons in optimized $CsPbBr_3$/g-C_3N_4 NHS was twice as long as that in the $CsPbBr_3$ NCs, leading to a higher probability of charge carriers participating in CO_2 reduction. Furthermore, TAS coupled with a PEC system has been employed to investigate the charge carrier dynamics in Au decorated

BiOI photocathode during the PEC H_2 evolution [34]. Findings revealed that the Au decoration effectively passivated BiOI surface states, resulting in the extended lifetime of photogenerated electrons in BiOI photocathodes and improved PEC H_2 evolution efficiency. Similarly, TAS coupled with PEC has also been used by Francàs et al. to investigate the impact of OEC decoration on hole dynamics in BVO photoanodes during PEC water oxidation [35]. Results demonstrated that the fast charge transfer from BVO to OEC suppressed charge recombination, resulting in improved PEC performance when OEC was modified on BVO photoanodes. Therefore, it is important to employ TAS for in-situ investigations of the effects of ov_s on charge carrier dynamics in BVO photoanodes during PEC water oxidation, as this area of research remains understudied.

In this study, we employed an easily scalable, low-power, non-thermal and less expensive technique called atmospheric pressure plasma jet (APPJ) as a post-treatment method for nanoporous BVO photoanodes. The characterization of scanning electron microscopy (SEM), X-ray diffraction (XRD), UV−visible absorption, Raman and time-resolved photoluminescence (TRPL) spectroscopies revealed that the bulk properties, including morphology, crystal structure, Eg, and charge carrier recombination for BVO remained unaltered after the APPJ treatment. However, the presence of ov_s layer was observed in the APPJ treated BVO photoanodes, as confirmed by X-ray photoelectron spectroscopy (XPS), Electron paramagnetic resonance (EPR) and high-resolution transmission electron microscopy (HR-TEM). The density of ov_s in BVO photoanodes could be controlled by adjusting the number of APPJ treatment cycles. The PEC properties of APPJ treated BVO photoanodes were evaluated using linear sweep voltammetry (LSV), incident photon-to-current conversion efficiency (IPCE), Absorbed photons to current conversion efficiency (APCE), Mott−Schottky plots, electrochemical impedance spectroscopy (EIS) and Bode plots. The results demonstrated a 3.4-fold improvement in photocurrent density of the APPJ treated BVO photoanodes compared to pristine BVO photoanode in PEC. This improvement can be attributed to the reduction of transfer resistance and charge carrier lifetime (τ_{ct}) at the BVO/electrolyte interface, achieved by introducing ov_s in BVO. This outcome promoted the hole transfer efficiency (η_{trans}) at BVO/electrolyte interface to enhance PEC performance of APPJ treated BVO photoanodes. To gain insights into the in-situ kinetics of charge carriers at BVO/electrolyte interface during PEC water oxidation, TAS combined with PEC cell was performed for the BVO photoanodes with and without APPJ treatment. The results revealed that the concentration and lifetime of trapped electrons were enhanced in ov_s states of the BVO photoanode with optimal APPJ treatment, while the concentration of surface holes also increased without affecting lifetime. These long-lived photoexcited electrons in the ov_s states of BVO photoanode effectively suppressed charge recombination at the BVO surface and facilitated hole transfer to electrolyte, leading to enhanced efficiency in PEC water oxidation. Furthermore, APPJ treated BVO photoanode with NiOOH/FeOOH OEC decoration demonstrated high photoactivity and stability in PEC water splitting. The optimal BVO photoanode exhibited a photocurrent density of 3.6 mA/cm^2 at 1.23 V_{RHE} and anodic bias photon-to-current efficiency (ABPE) of 1.4 % at 0.62 V_{RHE}. Faradaic efficiency (η_f) of H_2 and O_2 evolutions were measured 94 % and 93 %, respectively. The present study provides important and novel insights into the mechanisms underlying efficiency improvement to surface oxygen deficient BVO photoelectrodes for PEC applications.

2. Experimental methods

2.1. Preparation of BVO photoanodes

The two-step process was used to prepare the BVO photoanodes that has been reported in our pervious study [14]. Typically, the BIOI was coated on fluorine-doped tin oxide (FTO) substrate by electrodeposition in the first step. The plating solution was prepared by adding 0.664 g of

KI, 0.109 g of $Bi(NO_3)_3$ and 37.5 μL of HNO_3 in 5 mL deionized water (DI-H_2O) for sonication of 30 min. This solution was further mixed with 50 mg of *p*-benzoquinone, 0.25 mL of ethylene glycol and 1.75 mL of absolute ethanol to form a dark brown plating solution. The electrodeposition was performed by using FTO, Ag/AgCl and Pt as the working, reference and counter electrodes at − 0.25 V vs Ag/AgCl for 180 s to form BIOI on the FTO substrate in a three-electrodes system (Autolab, Metrohm PGSTAT204). The obtained BIOI electrodes were rinsed with DI-H_2O and ethanol and then dried with N_2 gas for the further using. For the second step, the 150 μL of 0.2 M vanadyl acetylacetonate solution (in dimethyl sulfoxide) was dropped on the BIOI electrode. The as-prepared electrode was calcined at 450 °C for 2 h under air atmosphere to form BVO electrode. As the BVO electrode cooled down to room temperature, it was soaked into a 1 M NaOH solution for 20 min to remove the excess V_2O_5 and then dried by N_2 for the further characterization. Note that the resulting BVO photoanode was denoted as Bare-BVO.

2.2. Post-treatment of BVO photoanodes using APPJ

The as-prepared Bare-BVO samples with a feature dimension of 1.5 cm × 2.0 cm were post-treated by APPJ (Creating Nano Technologies Inc., Atmospheric Pressure Plasma SAP009SA) under a mixed gas (95 % of N_2 and 5 % of H_2) flow of 8.5 L/min under atmospheric environment at room temperature. The distance between the jet and the BVO samples was maintained at 1.6 cm during the exposure for 24/48/72/96 scan cycles. The resulted BVO photoanode samples were denoted as P-24-BVO, P-48-BVO, P-72-BVO and P-96-BVO, respectively.

2.3. OEC deposition on BVO photoanodes

The OEC, FeOOH and NiOOH layer was sequentially coated on the surface of BVO photoanode samples (Bare-BVO and P-72-BVO) by photoelectrodeposition that has been reported in the literature [36]. The mixed aqueous solution contained 5 mM of $FeSO_4$·7 H_2O and 100 mM of K_2SO_4 was purged with N_2 for 30 min to serve as the plating solution for FeOOH photodeposition on the surface of BVO. The Bare-BVO and P-72-BVO samples were used as the working electrodes, respectively, and Ag/AgCl and Pt were used as the reference and counter electrodes in the three-electrodes system coupled with a light source (300 W Xe lamp with a light intensity of 3 mW/cm^2). The applied voltage was 0.539 V vs Ag/AgCl and the period of time was 150 s for the FeOOH photodeposition. The obtained samples were rinsed with DI-H_2O and then dried by N_2 for the further utilization. On the other hand, the 50 mM of $NiSO_4$·6 H_2O and 100 of mM K_2SO_4 aqueous solutions were individually prepared. The samples coated with FeOOH were firstly soaked in the $NiSO_4$·6 H_2O aqueous solution for 10 min and then moved to K_2SO_4 aqueous solution for the photodeposition at 0.029 V vs Ag/AgCl for 90 s. The resulted samples were rinsed with DI-H_2O and then dried by N_2. The procedure of FeOOH photodeposition was repeated one more time to obtained the FeOOH and NiOOH layer coated BVO photoanode samples which were denoted as Bare-BVO-NF and P-72-BVO-NF.

2.4. Characterizations

Morphological analysis of the as-prepared BVO photoanodes were performed using high-resolution field-emission SEM (HITACHI SU-5000). The crystalline phase of the as-prepared BVO samples was investigated using XRD (Rigaku Americas Miniflex Plus powder diffractometer) at the voltage of 40 kV and current of 30 mA. The scanning angle range was 10–80° (2θ) with a rate of 5°/min. Alpha Step IQ (KLA TENCOR) was used to measure the film thickness of the BVO on FTO. HR-TEM and energy-dispersive X-ray spectroscopy (EDX) was carried out to investigate the lattice spacing and elemental distribution of the BVO samples using JEOL JEM-2100 F Field Emission Gun TEM. A micro-spectrometer (RLS1000, Rainbow-Light) coupled with an integrating sphere was used to collect the UV–visible absorption spectra of the BVO photoanodes. TRPL spectra were collected using a single-photon counting system (Pico Quant PDL 800-B) with a GaN diode laser (λ = 375 nm, 50 ps pulse duration) as the excitation source to study the charge carrier recombination dynamics of the BVO at 575 nm [14]. XPS spectra of the BVO electrodes were obtained by Thermo Fisher Scientific ESCALAB Xi+ electron spectroscopy with Al Kα1 anode. EPR measurements were carried out on Bruker EMX-Plus 10/12, X-band.

2.5. PEC measurements for BVO photoanodes

The bare FTO part of the BVO photoanodes was welded with a conductive wire and sealed with insulating epoxy resin, resulting in an exposed surface of 1.2×1.0 cm^2. The as-prepared samples were used as working electrodes for PEC measurements, within Pt and Ag/AgCl were used as counter and reference electrodes, respectively. A 1 M H_3BO_3 aqueous solution with pH of 9.5 was used as the electrolyte. LSV, chronoamperometry, EIS (frequency range of 100 kHz to 0 Hz), Bode plots and Mott-Schottky (measured under 1 kHz) plots were examined by Autolab (PGSTAT204) under simulated sunlight (Excelitas HX22, 300 W Xe lamp coupled with AM 1.5 and infrared water filter). IPCE was collected using the Autolab with a solar simulator (HORIBA PowerArc) coupled with an aligned monochromator (HORIBA TRIAX 180). The gas evolution of PEC water splitting was performed in a gas-tight reactor within the nafion membrane to separate the BVO photoanodes and Pt electrodes for carrying out O_2 and H_2 evolutions, respectively. The examined gases were collected using a gas-tight syringe and analyzed by a gas chromatograph (SHIMADZU GC-2010, BID-2010 plus). The calculations of V_{RHE} potential, η_{trans}, charge separation efficiency (η_{sep}), η_f, ABPE, IPCE and APCE are shown in supporting information.

## 2.6. TAS measurements of Bare-BVO and P-72-BVO in PEC cell

The TAS using a home-built system consists of a Nd:YAG laser (LOTIS LS-2134, 8 ns pulse width) coupled with wavelength tunable system (LOTIS LT-2211) at 390 nm as the pump beam; the frequency of the laser flash was 10 Hz; the intensity of laser pulse was 200 μJ/cm^2 [34]. The probe light source was 150 W Xe lamp (GLORIA-X150A) equipped with band-pass filters within the bandwidth of 10 nm (Andover Corporation). The center wavelength of used band-pass filters was 500, 523, 550, 577, 600, 630, 650, 675 and 700 nm, respectively. The pump and probe beams were aligned on the surface of working electrode (Bare-BVO and P-72-BVO) in the PEC cell that composed with Pt and Ag/AgCl as the counter and reference electrodes, and H_3BO_3 aqueous solution (pH 9.5) as the electrolyte. A silicon photodiode (Zolix DSi 200) was used to detect transmitted photons. Collected data were processed by a digital delay/pulse generator (Stanford Research Systems, DG535) and recorded with an oscilloscope (GDS-2302A) on the timescale of μs. The TAS signals were recorded when the applied voltage of PEC cell was set at 1.23 V_{RHE}.

3. Results and discussion

3.1. Morphological, crystal, optical and surface chemical properties of BVO photoanodes with APPJ post-treatment

Fig. 1a presents the SEM images of the Bare-BVO and the BVO samples with APPJ treatment. All the samples exhibit a coral-like morphology with nanopores. Notably, after APPJ post treatment, a slightly roughened surface was observed on the BVO photoanode samples without significant changes to morphology. Film thicknesses of all BVO photoanode samples are shown in Fig. S1, revealing a consistent thickness of approximately 250 nm. XRD spectra were collected to investigate the effect of APPJ treatment on the crystal structures of the BVO photoanode samples. Fig. 1b shows that all the samples exhibit similar XRD patterns, indicating the presence of monoclinic-phase $BiVO_4$. Furthermore, UV–visible absorption spectra were recorded for
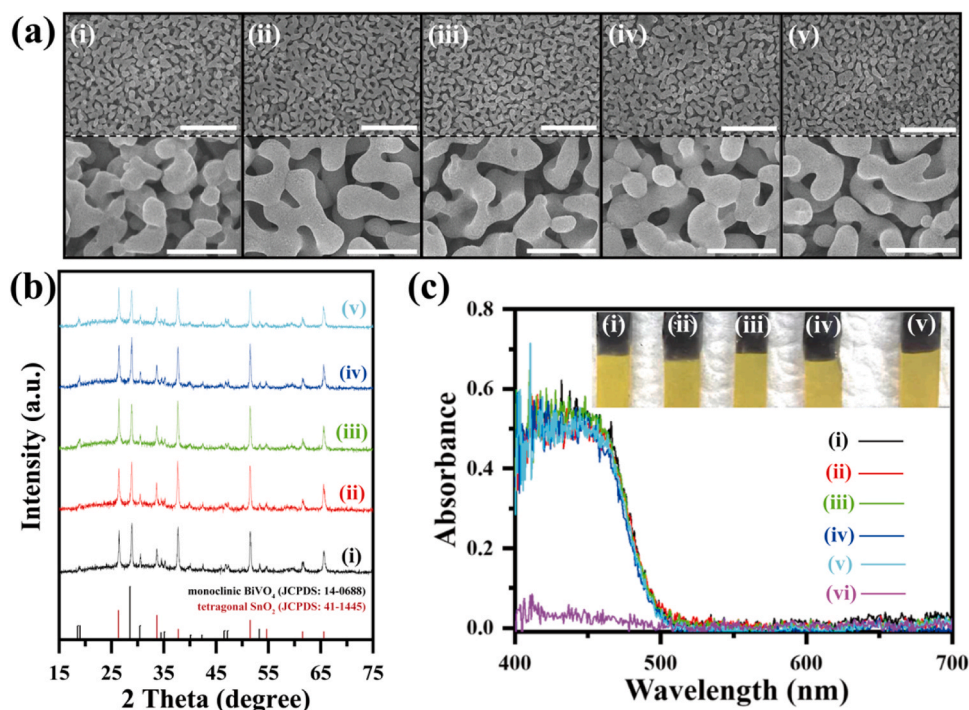
Fig. 1. (a) SEM images (top: low magnification images and the scale bars are 5 μm; bottom: high magnification images and the scale bars are 200 nm), (b) XRD patterns (the standard patterns of monoclinic BVO and tetragonal SnO_2 (FTO) are incorporated for comparison) and (c) UV–visible absorption spectra (inset: photographs of the BVO photoanode samples) of (i) Bare-BVO, (ii) P-24-BVO, (iii) P-48-BVO, (iv) P-72-BVO and (v) P-96-BVO (vi) FTO substrate.
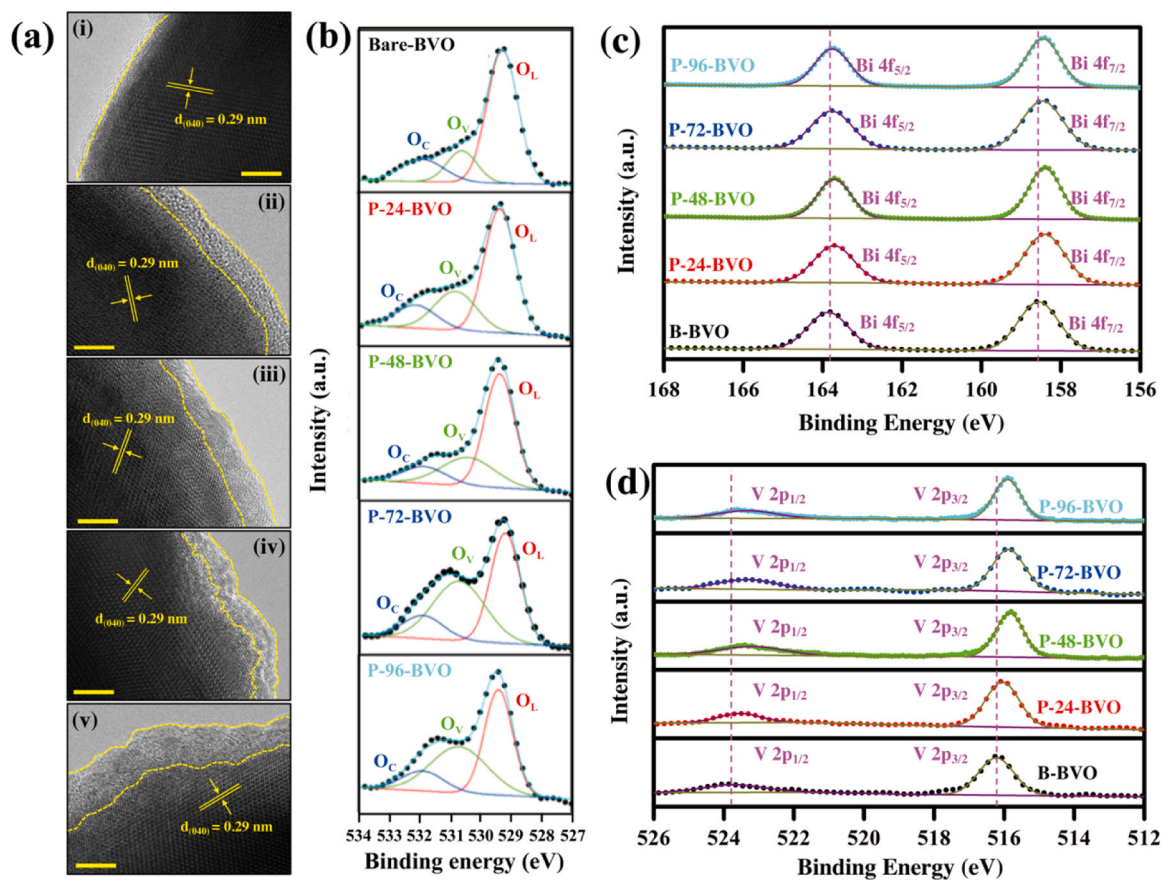
Fig. 2. (a) HR-TEM images of (i) Bare-BVO, (ii) P-24-BVO, (iii) P-48-BVO, (iv) P-72-BVO and (v) P-96-BVO. (b) O 1 s, (c) Bi 4 f and (d) V 2 p XPS spectra of Bare-BVO, P-24-BVO, P-48-BVO, P-72-BVO and P-96-BVO.

all the BVO photoanode samples and the FTO substrate to explore variations in their optical properties following APPJ treatment. Interestingly, Fig. 1c illustrates that all the BVO photoanode samples display similar absorption profiles in the range of 400–550 nm, corresponding to the band-to-band electronic transition of the typical $BiVO_4$ [14]. The E_g values of all the BVO photoanode samples can be estimated as 2.51 eV using tauc plots derived from the UV–visible absorption spectra (Fig. S2). Notably, the BVO photoanodes appear slightly darker yellow after the APPJ treatment compared to the pristine BVO photoanode, which differs significantly from the blackened BVO photoanodes reported in the literature following plasma treatment [21]. These results suggest that APPJ post-treatment does not significantly affect the morphology, crystal structure, or optical properties in BVO. The slightly difference in color may be attributed to the surficial variation of BVO due to APPJ treatment.

To confirm changes in the surface properties, HR-TEM images of the Bare-BVO and BVO photoanodes with APPJ treatment were obtained. As shown in Fig. 2a, the Bare-BVO exhibits a well-crystalline with a smooth surface displaying clear lattice fringes on the (040) crystal plane. In contrast, the BVO photoanodes with APPJ treatment also present a well-crystalline structure but show a rougher surface with an amorphous layer. The thickness of amorphous layer is estimated as 2–4 nm for the P-24-BVO, P-48-BVO, P-72-BVO and P-96-BVO. XPS characterization was further performed to gain further insights into the surficial chemical states of BVO photoanodes after APPJ treatment. The XPS analysis results are presented in Figs. 2b-2e. The O 1 s XPS spectra exhibited an asymmetrical peak that can be fitted into three components: lattice oxygen (O_L) at 529.3 eV, oxygen deficiencies (O_V) at 530.2 eV and chemisorbed water molecules (O_C) at 531.7 eV [28]. The contribution of O_v enhances while that of O_L decreases with an increasing number of APPJ treatment cycles, as shown in Table S1. The contribution of O_v is evaluated as 15 %, 25 %, 26 %, 42 % and 40 % for the Bare-BVO, P-24-BVO, P-48-BVO, P-72-BVO and P-96-BVO. In addition, a shift toward lower bonding energy is observed in the Bi 4 f and V 2p XPS spectra when comparing the Bare-BVO with the APPJ-treated BVO photoanode samples. The Bi 4 f XPS spectra of all BVO samples can be fit into the symmetric peaks, indicating as the valence state of Bi in the BVO is mainly Bi^{3+} without the Bi defects [37]. However, the V $2p_{3/2}$ in XPS spectra can be fit into a major peak of V^{5+} and a minor peak V^{4+} as shown in the Fig. S3 [31]. Their contributions are also measured and listed in Table S1. For the Bare-BVO, the valence state of V is 97.7 % of V^{5+} and 2.3 % of V^{4+}. After the APPJ treatment, the contribution of V^{4+} slightly increases to 2.7 %, 3.1 %, 4.8 % and 4.4 % for P-24-BVO, P-48-BVO, P-72-BVO and P-96-BVO. These results reveal that the 72-cycled APPJ treatment with 5 % of H_2 plasma would act as a weak reducing agent toward surface oxygen, producing saturated ov_s in the BVO without damaging its microstructure [38]. The 96-cycled APPJ treatment may generate the unexpected defect states in the BVO photoanodes, resulting in the negative effects in the PEC application [37]. In addition, the formation of ov_s in the BVO by the optimal APPJ treatment would not accompany with the significant variation in valence states of V and Bi and Bi/V ratio (Table S2). The changing of the local coordination environments of V and Bi atoms may also increase electron density of BVO photoanodes to improve the performance in PEC application [21]. For the further comprehensive comparison of the ov_s in the BVO photoanode samples, EPR spectra of Bare-BVO, P-24-BVO, P-48-BVO, P-72-BVO, and P-96-BVO were collected (Fig S4). The trend of signal intensity of oxygen vacancies is P-72-BVO > P-96-BVO > P-48-BVO > P-24-BVO > Bare-BVO, which confirms the APPJ treatment is a facile method to produce oxygen vacancies in the BVO photoanodes.

Since the APPJ treatment only change the surface properties without altering the bulk crystal structure in BVO, the Raman and TRPL spectroscopies were performed on the Bare-BVO and P-72-BVO to further confirm this contention. As shown in Fig. S5a, no significant differences were observed in the Raman spectra between the Bare-BVO and P-72-

BVO samples, indicating that both samples exhibit similar vibrational bands without any degradation to their crystalline structure. Additionally, the PL emission lifetime measurements (Fig. S5b) revealed a similar decay behavior for the Bare-BVO and P-72-BVO samples. However, a slightly increased fast decay component was observed for the P-72-BVO sample, suggesting an improvement in the surface trapping of the photoexcited charge carriers before bulk recombination [39,40]. These findings, along with the HR-TEM, XPS and EPR results, indicate that APPJ treatment solely induces ov_s in the BVO photoanodes without compromising their bulk properties. This ov_s may serve as a shallow donor to increase charge carrier concentration and facilitate chemical species adsorption, leading to the enhanced photoactivity of the BVO photoanodes in PEC water oxidation [10]. Consequently, the PEC characterization of the as-prepared BVO photoanodes was further examined as described below.

3.2. PEC water oxidation performance of BVO photoanodes with APPJ post-treatment

PEC measurements for the BVO photoanode samples were conducted using a three-electrode cell with Pt wire and Ag/AgCl as counter and reference electrodes, respectively. The LSV curves of Bare-BVO, P-24-BVO, P-48-BVO, P-72-BVO and P-96-BVO under dark conditions and solar simulated light irradiation at 100 mW/cm^2 are depicted in Figs. 3a-3b. The dark scans within the range of 0.17–1.23 V_{RHE} for all BVO photoanode samples displayed negligible currents ($\sim 10^{-8}$ mA/cm^2). Consequently, when irradiation light was applied, all tested samples exhibited apparent photo-responses within the same scan range. Photocurrent densities at 1.23 V_{RHE} were measured as 1.0, 2.4, 2.7, 3.4 and 3.0 mA/cm^2 for Bare-BVO, P-24-BVO, P-48-BVO, P-72-BVO and P-96-BVO, respectively, in the borate buffer electrolyte. In addition, onset potential of the photocurrent for the APPJ treated BVO photoanodes showed significant shift towards a lower potential of 0.32 V_{RHE} as compared to that of the Bare-BVO (0.57 V_{RHE}). These improvements in photocurrent density and lowered onset potential demonstrate the effective enhancement of photoactivity in BVO photoanodes for PEC water oxidation through APPJ treatment. Moreover, upon incorporation of a hole scavenger (Na_2SO_3) into the electrolyte, all the tested BVO photoanode samples showed the similar photocurrent densities of approximately 3.6 mA/cm^2 at 1.23 V_{RHE}. These results indicate that the introduction of ov_s in the BVO photoanodes by APPJ treatment influences the hole transfer behavior at the interface between BVO and electrolyte. Consequently, the charge separation efficiency (η_{sep}) and charge transfer efficiency (η_{trans}) of the BVO photoanode samples were calculated and are shown in Figs. 3c-3d. The η_{sep} for all the tested BVO photoanode samples shows the equivalent values of approximately 70 % at 1.23 V_{RHE}. However, the η_{trans} values are estimated as 27 %, 68 %, 75 %, 95 % and 82 % at 1.23 V_{RHE} for Bare-BVO, P-24-BVO, P-48-BVO, P-72-BVO and P-96-BVO, respectively. These results illustrate that the hole transfer performance of BVO photoanodes can be significantly improved about 3.5-fold by creating ov_s using APPJ. To gain insights into the factors contributing to enhanced photoactivity of BVO photoanodes due to ov_s, IPCE spectra were collected for Bare-BVO, P-24-BVO, P-48-BVO, P-72-BVO and P-96-BVO. As depicted in Fig. 3e, all BVO photoanode samples exhibit similar profiles within the range of 300–600 nm in the IPCE spectra. This phenomenon indicates that charge collection primarily occurs from the conduction band (CB) and VB of BVO without defect-induced E_g reduction that has been reported in the literatures [21,41]. A 2.3-fold improvement in efficiency was observed via the creation of ov_s when comparing the performance of Bare-BVO and P-72-BVO at 450 nm. Additionally, the IPCE was converted into APCE for all the BVO photoanode samples, as shown in Fig. 3f, revealing a significant improvement in APCE from 29 % to 70 % at 450 nm for the BVO photoanode after APPJ treatment.

To gain a better understanding of APPJ treatment on BVO photoanodes when improving efficiency in PEC water oxidation, Mott-
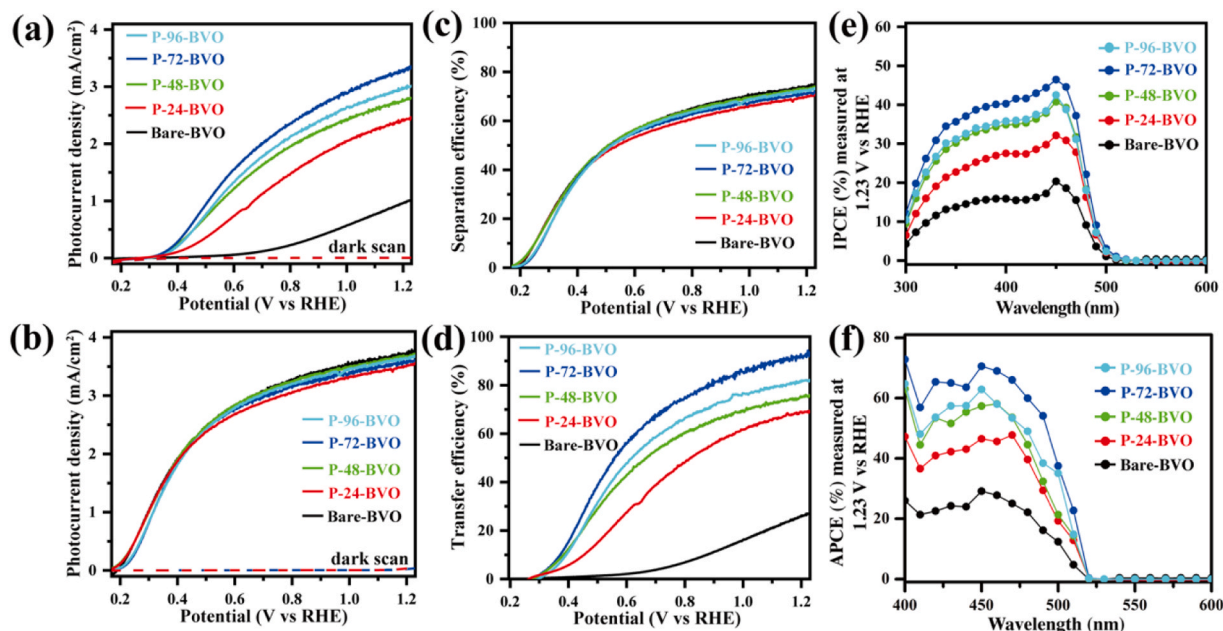
Fig. 3. LSV curves in H_3BO_3 aqueous solution (a) without and (b) with a hole scavenger ($[Na_2SO_3] = 0.2$ M), (c) η_{sep}, (d) η_{trans}, (e) IPCE and (f) APCE spectra of the BVO photoanode samples.

Schottky, EIS and Bode plots were performed on the BVO photoanode samples. Mott-Schottky plots in Fig. 4a shows that the flat-band potential (E_{fb}) of Bare-BVO, P-24-BVO, P-48-BVO, P-72-BVO and P-96-BVO is measured as 2.31, 2.38, 2.45, 2.50 and 2.48 V_{RHE}. A slight anodic shift in the E_{fb} of the BVO photoanode can be observed after APPJ treatment. Additionally, the charge carrier concentration can be estimated as 1.68×10^{20}, 1.76×10^{20}, 2.01×10^{20}, 2.39×10^{20} and 2.23×10^{20} cm^{-3} for Bare-BVO, P-24-BVO, P-48-BVO, P-72-BVO and P-96-BVO, respectively. These values reveal that the electronic band structure and donor density of the BVO photoanode are slightly altered by the creation of ov$_s$ using APPJ. Since the ov$_s$ is produced at the surface of the BVO photoanode, it is important to study the charge transfer properties at the

BVO/electrolyte interface. Therefore, the EIS spectra of BVO photoanode samples were collected in the PEC cells under light illumination. As shown in Fig. 4b, the interfacial charge transfer properties at the BVO/electrolyte interface are improved after the creation of ov$_s$ in the BVO photoanodes by APPJ. To quantify these interfacial charge transfer properties, the EIS spectra are fitted by an equivalent circuit (inset of Fig. 4b) and the parameters are summarized in Table S3. A significant reduction in charge transfer resistance was observed from 3.4 to 0.2 kΩ for the BVO photoanodes with the optimal APPJ treatment. Furthermore, Bode plots are used to calculate the lifetime of charge transfer at the BVO/electrolyte interface using the expression ($\tau_{ct} = 1/2\pi f_{max}$) [34]. As shown in Fig. 4c, the τ_{ct} values for Bare-BVO, P-24-BVO, P-48-BVO,
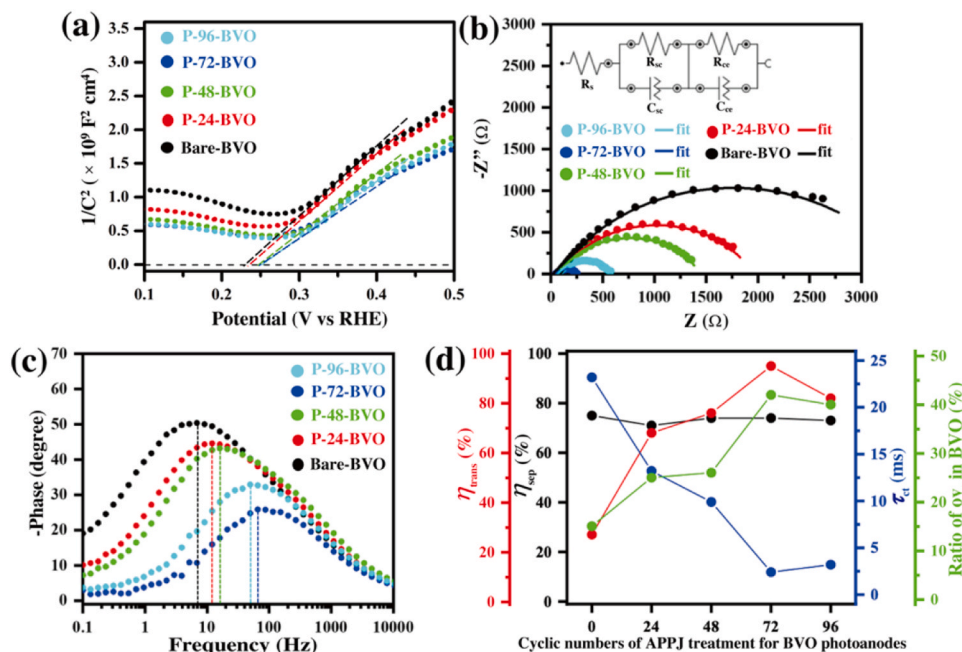

Fig. 4. (a) Mott-Schottky, (b) EIS and (c) Bode plots of Bare-BVO, P-24-BVO, P-48-BVO, P-72-BVO and P-96-BVO. (d) The correlation between η_{trans}, η_{sep}, τ_{ct}, ratio of ov$_s$ in BVO and the cyclic numbers of APPJ treatment for BVO photoanodes.

P-72-BVO and P-96-BVO are calculated as 23.2, 13.2, 9.9, 2.4, and 3.2 ms, respectively. These results indicate that the ov_s in BVO, created by APPJ treatment, significantly reduce the transfer resistance and τ_{ct} of charge carriers at the BVO/electrolyte interface, promoting the efficiency in PEC water oxidation [42]. To interpret the effects of ov_s in BVO on PEC properties, the number of APPJ post-treatment cycles is correlated with η_{sep}, η_{trans}, τ_{ct} and ratio of ov_s in BVO, as summarized in Fig. 4d. As the number of APPJ post-treatment cycles increased from 24 to 72, the ratio of ov_s in the BVO photoanode increased by approximately 2.8 times. The η_{trans} of photoexcited holes in the BVO photoanode increased from 27 % to 95 %, resulting in a shortened τ_{ct} from 23.2 to 2.4 ms. However, with 96 cycles of APPJ post-treatment, the ratio of ov_s in the BVO photoanode decreased. A simultaneous reduction in η_{trans} and lengthening of τ_{ct} in the BVO photoanode are also observed. This hindering phenomenon may be attributed to the saturation of ov_s and generation of other unexpected defects in the BVO photoanode due to excessive APPJ post-treatment. These unexpected defect states in the BVO photoanode may serve as the recombination center of charge carriers to inhibit the PEC activity [37,43]. Interestingly, stable values of η_{sep} among BVO photoanodes suggest that the charge separation behavior mainly relies on the bulk properties of BVO and is not significantly affected by the APPJ post-treatment. Based on these results, it can be concluded that the present APPJ post-treatment using an optimal 72 cycles can produce sufficient ov_s in BVO photoanodes to enhance interfacial hole transfer, leading to the improvements in photoactivity of PEC water oxidation.

3.3 In-situ investigation of the charge carrier dynamics at the interface between APPJ treated BVO photoanodes and electrolyte during PEC water oxidation.

It is important to explore the role of charge carriers in practical PEC water oxidation by investigating the influence of ov_s on charge transfer behavior at the BVO/electrolyte interface. Therefore, TAS coupled with working PEC cells were used to directly monitor the dynamics of photogenerated charge carriers in the BVO photoanodes during water

oxidation [34]. Herein, TAS signals from BVO photoanodes were recorded at 1.23 V_{RHE} (at which water oxidation was expected to take place) using 390 nm pump and white light probe (500–700 nm) with varying time delays between pump and probe. The wavelength-dependent TAS for Bare-BVO and P-72-BVO at different delay times are presented in Figs. 5a and 5b. For both BVO samples, similar TAS features with varied amplitudes at different delay times were observed. The transient bleach (TB) at shorter wavelengths (< 550 nm) and transient absorption (TA) in the 550–700 nm range, respectively, are implicated as the trapped electron in the ov_s states and the accumulated hole on the surface of BVO photoanodes during photo-induced oxidation [35]. Fig. 5c compares the recovery of TB signals at 500 nm for Bare-BVO and P-72-BVO. A larger TB amplitude is observed for P-72-BVO when compared to Bare-BVO. Furthermore, TB recoveries can be fitted as 29 and 7 μs for P-72-BVO and Bare-BVO, respectively. These results indicate that a higher concentration of photoexcited electrons is trapped in the ov_s states with a longer lifetime in P-72-BVO, consistent with earlier findings that P-72-BVO exhibited a higher density of ov_s. Conversely, TA decays at 650 nm for P-72-BVO and Bare-BVO are shown in Fig. 5d. The amplitude of the TA signal of P-72-BVO is larger as compared to that of Bare-BVO, while both samples exhibit the same lifetime of ~14 μs. This suggests that the kinetics of surficial holes involved in water oxidation are similar for BVO with or without the ov_s layer. However, the higher concentration of surficial holes in P-72-BVO can be attributed to electron trapping on the ov_s layer, leading to the strong suppression of charge carrier recombination through surface states. These outcomes facilitate the apparent enhancement of η_{trans} at the interface between BVO and electrolyte.

Based on the findings from TAS and PEC experiments, a plausible mechanism for the improved efficiency of PEC water oxidation in BVO photoanodes treated with APPJ can be proposed, as illustrated in Fig. 6. For the pristine BVO photoanode (Bare-BVO), the electrons and holes generated on the CB and VB under illumination. Some of these charge carriers are trapped in trap states, including shallow electron traps for
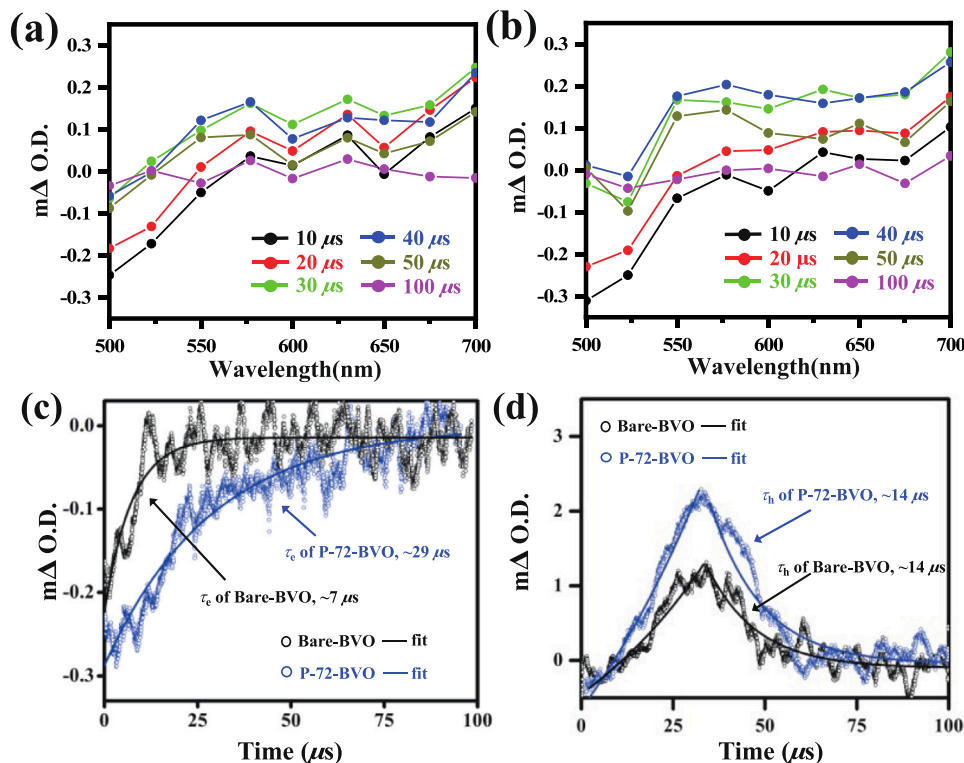
Fig. 5. Full TAS profiles of (a) Bare-BVO and (b) P-72-BVO at varied delay time between pump and probe under working PEC at 1.23 V_{RHE}. (c) TB recovery (probing at 500 nm) and (d) TA decay (probing at 650 nm) profiles of Bare-BVO and P-72-BVO.
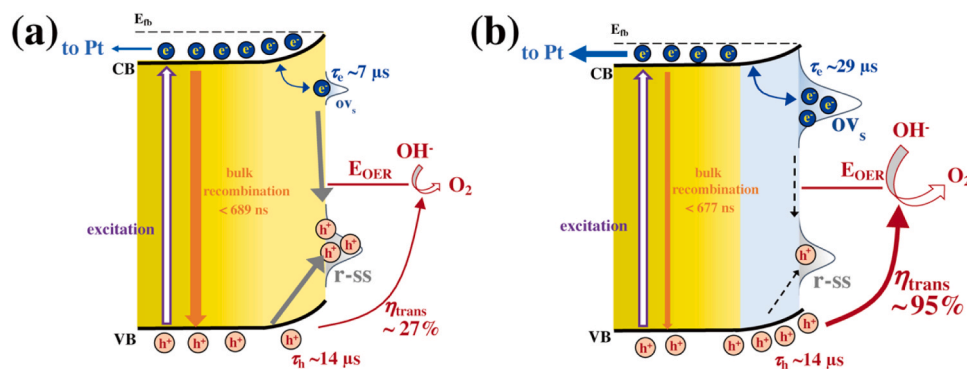
Fig. 6. Schematic illustration for the proposed assignment of charge carrier dynamics of (a) Bare-BVO and (b) P-72-BVO in PEC water oxidation.

ov_s or hole trap states like VO^{2+}/VO_2^+ (recombination surface states, r-ss) [44], occurring on a picosecond time scale [45]. Additionally, some charge carriers recombine from CB to VB or in trap states through a radiative pathway with lifetime of approximately 670–690 ns. The electrons trapping in ov_s is reversible under bias, resulting in migration of the electrons to the counter electrode (Pt) in H_2 evolution [31]. However, the trapped holes in r-ss would recombine with electrons via a none-radiative pathway, resulting in a lifetime (τ_e) in ov_s of only about 7 μs. The remaining holes diffuse to the surface to facilitate O_2 evolution with a lifetime (τ_h) of approximately 14 μs and a η_{trans} of 27 %, which results in a poor efficiency for Bare-BVO in PEC water oxidation.

Following optimal APPJ treatment, the bulk properties of BVO photoanode (P-72-BVO) remain similar to those of pristine BVO photoanode (Bare-BVO), including the E_g, crystal structure, and bulk recombination of charge carriers. However, the density of ov_s significantly increases, as confirmed by HR-TEM, XPS and EPR characterization. Lifetime and concentration of trapped electrons in the ov_s states are both enhanced, with τ_e prolonged to approximately 29 μs. Consequently, the increased ov_s density would improve the electron trapping, leading to the suppression of the recombination with hole in r-ss of BVO. As the concentration of the trapped hole saturated in r-ss, the remining holes would accumulate on the surface without recombination, facilitating the η_{trans} to achieve 95 % at BVO/electrolyte interface. However, the τ_h of surface holes in P-72-BVO during water oxidation remains similar, which may attribute to the slow kinetics of O_2 evolution [6,46]. In addition, H_2O molecules are more likely to adsorb onto the V sites surrounding the ov_s, thereby reducing the energy required for OH* intermediate formation, leading to an enhanced activity of BVO in PEC water oxidation [10,27,28]. These outcomes improve the charge transfer efficiency at the BVO/electrolyte interface and the photoactivity toward water oxidation for the APPJ-treated BVO photoanodes in PEC application.

3.3. Chemical stability and performance examinations of APPJ-treated BVO photoanodes with OEC decoration in PEC water splitting

To highlight the advantages of the APPJ treatment, stability of Bare-BVO and P-72-BVO in PEC water oxidation was examined. Fig. S6 shows that the photocurrent decay ratio was approximately 75 % and 90 % after ten minutes and one hour, respectively, for Bare-BVO. In contrast, P-72-BVO exhibited significantly lower decay ratios of only 23 % and 73 % during the same examination periods under identical conditions. The observed decay to photocurrent can be attributed to the dissolution of V^{5+} from the BVO lattice [36], which indicates poor chemical stability of Bare-BVO in PEC water oxidation. On the other hand, the improved stability was observed in P-72-BVO, suggesting that the ov_s induced remarkable interfacial charge transfer properties would inhibit the dissolution of V^{5+} in BVO. However, despite improved performance of P-72-BVO, it remains unsuitable for practical application in PEC water splitting given insufficient chemical stability. To address the issue of

chemical stability, a NiOOH/FeOOH OEC was further decorated on P-72-BVO (sample denoted as P-72-BVO-NF). The decoration of NiOOH/FeOOH OEC on P-72-BVO was carried out by using photo-electrodeposition method [36]. Fig. 7a shows a HR-TEM image that an amorphous layer with a thickness about 5–7 nm is coated on the BVO surface. Note the clear crystalline fringes still can be observed at the inner BVO, which indicates that the photoelectrodeposition process does not affect the crystallinity or crystal structure of BVO. To further confirm the composition of the presented amorphous layer on the surface of BVO, the TEM EDS line-scan was collected and is shown in Fig. S7. The significant signals of Fe and Ni are measured at the outer layer and the Bi, V, and O signals are observed mainly at the inner domain, evidencing the NiOOH/FeOOH OEC layer is successfully decorated on the surface of BVO. In addition, the amorphous interfacial part between outer OEC layer and inner crystalized BVO shows the overlapped signals of Bi, V, O, Fe and Ni, which may be suggested that the mixed composition of BVO ov_s and NiOOH/FeOOH OEC. This outcome indicates that the ov_s layer would still exist and present its function after OEC decoration for BVO photoanodes. Furthermore, the TEM-EDS mapping of the P-72-BVO-NF in Fig. 7b demonstrated a uniform distribution of Ni and Fe elements around the BVO surface, revealing a homogeneous coating of NiOOH/FeOOH OEC on the APPJ treated BVO photoanode.

The PEC performance of P-72-BVO-NF was further evaluated and compared with Bare-BVO and P-72-BVO. As shown in Fig. 7c, the LSV profiles demonstrate that the P-72-BVO-NF exhibits a higher photocurrent density than P-72-BVO and Bare-BVO within the same bias scan range under illumination. The photocurrent density of P-72-BVO-NF can achieve 3.6 mA/cm^2 at 1.23 V_{RHE}. Moreover, P-72-BVO-NF shows a lower unset potential of photocurrent (0.25 V_{RHE}) as compared to P-72-BVO and Bare-BVO. On the other hand, the APCE of P-72-BVO-NF was measured as 77 % at 450 nm, as shown in Fig. S8. These outcomes suggest that the presence of NiOOH/FeOOH OEC assist in hole extraction from BVO to electrolyte, increasing the photoactivity of APPJ-treated BVO photoanode in PEC water oxidation [46]. In addition, the ABPE was calculated for P-72-BVO-NF, P-72-BVO and Bare-BVO, resulting in the individual maximum value of 1.4 % at 0.62 V_{RHE}, 1.1 % at 0.69 V_{RHE} and 0.1 % at 0.96 V_{RHE}, respectively. These calculation results indicate that the creation of ov_s in BVO by APPJ dramatically improves the ABPE by approximately one order and reduces optimal applied voltage by around 0.27 V (from 0.96 V_{RHE} to 0.69 V_{RHE}). Moreover, the incorporation of the NiOOH/FeOOH OEC on the APPJ-treated BVO photoanode further enhances the ABPE by 1.3-fold and reduces the applied voltage to 0.62 V_{RHE} in PEC water oxidation. Furthermore, the chronoamperometric I−t curves of P-72-BVO-NF, P-72-BVO and Bare-BVO under chopped light irradiation at 1.1 V_{RHE}, as shown in Fig. 7d, demonstrate that the P-72-BVO-NF exhibits a more stable photocurrent as compared to P-72-BVO and Bare-BVO. Consequently, the practical PEC water splitting of P-72-BVO-NF was performed to demonstrate the benefits of NiOOH/FeOOH OEC decoration and APPJ treatment for BVO photoanodes in the PEC cell at 0.62 V_{RHE}.
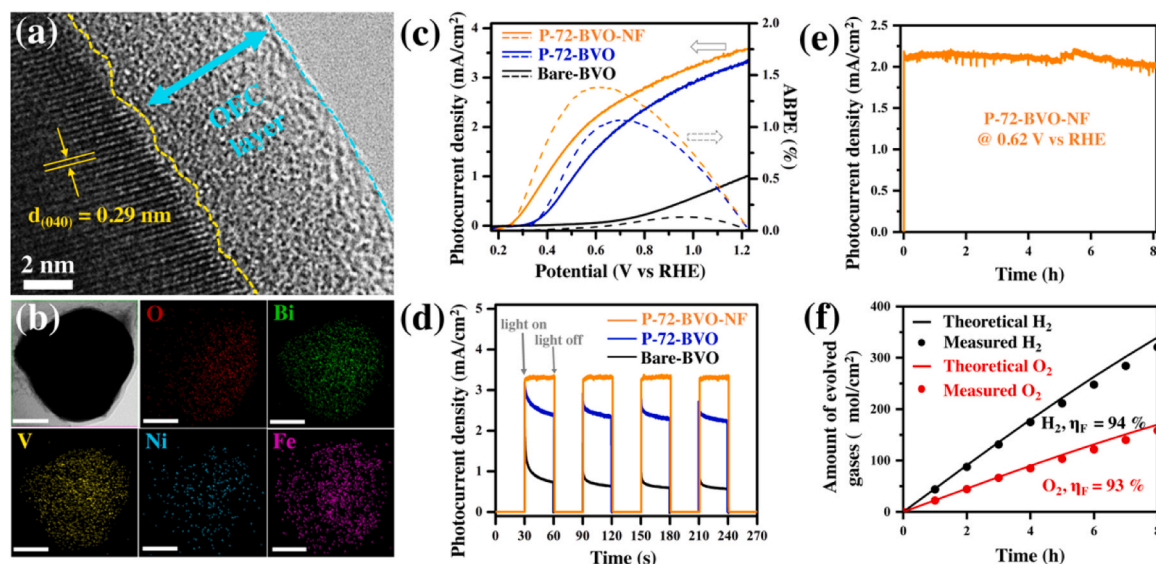
Fig. 7. (a) HR-TEM image and (b) TEM-EDS mapping of P-72-BVO-NF (scale bars are 100 nm). (c) LSV curves and ABPE profiles, and (d) chronoamperometric I–t curves of P-72-BVO-NF, P-72-BVO and Bare-BVO under chopped light irradiation at 1.1 V$_{RHE}$. (e) chronoamperometric I–t plot of the P-72-BVO-NF at 0.62 V vs RHE. (f) H$_2$ and O$_2$ evolution produced by the P-72-BVO-NF photoanode at 0.60 V vs RHE and calculated H$_2$ and O$_2$ amount from the photocurrent density in (e).

As depicted in Fig. 7e, no significant decay in photocurrent was observed during the 8-hour examination. The gas evolution experiments were conducted using GC to confirm the O$_2$ evolution at P-72-BVO-NF photoanode and the H$_2$ evolution at the Pt electrode. Fig. 7f compares the measured gas evolution amount with the theoretical gas generation rates that calculated based on photocurrent density achieved by P-72-BVO-NF. The rates of H$_2$ and O$_2$ evolutions were measured as 40.3 and 19.8 μmol/cm^2 h, respectively, for P-72-BVO-NF. The ratio between the H$_2$ and O$_2$ productions is close to 2:1. Moreover, the η_f of H$_2$ and O$_2$ evolutions at 0.62 V$_{RHE}$ were found to be 94 % and 93 %, respectively, indicating that the observed photocurrent of P-72-BVO-NF substantially contributes to water splitting. To demonstrate the potential of P-72-BVO-NF in the practical application of PEC water splitting, the long-term examination of 50 h was further performed. As shown in Fig. S9, no significant decay in the photocurrent density of P-72-BVO-NF is observed. The morphology and crystal structure of P-72-BVO-NF remain the same after the long-term examination. These outcomes highlight the remarkable chemical stability of P-72-BVO-NF in PEC water splitting. Note that the film thickness of P-72-BVO-NF is only about 250 nm, which is thinner than the reported thickness (0.7–1.5 μm) in the literatures [21,44,47]. While the photocurrent density of P-72-BVO-NF remains relatively low compared to reported studies, it is anticipated that its performance will be further improved by using a thicker BVO film coupled with APPJ treatment. These findings reveal the highly efficient and stable PEC water oxidation is accomplished by BVO photoanodes with APPJ treatment and subsequent NiOOH/FeOOH OEC decoration. The enhanced PEC water splitting capability is achieved by the creation of high density ov$_s$ in BVO photoanodes, which promotes the charge transfer efficiency at BVO/electrolyte interface for the practical applications in photoelectrical conversion.

4. Conclusion

A high density of shallow ov$_s$ in BVO photoanodes was successfully demonstrated through APPJ post-treatment. This treatment preserved their bulk properties of BVO photoanodes. The optimized BVO photoanode (P-72-BVO) exhibited a remarkable 3.4-fold improvement in photocurrent density compared to the pristine BVO photoanode (Bare-BVO) in PEC water oxidation. Such significant enhancement to PEC performance can be attributed to an exceptional charge transfer property with a short τ_{ct} of 2.4 ms at the BVO/electrolyte interface for P-72-BVO. By employing TAS coupled with a PEC cell, in-situ investigations of charge carrier dynamics at the BVO/electrolyte interface during water oxidation were conducted. The results revealed that the long-lived electrons could be effectively trapped in the ov$_s$ states, thereby suppressing charge recombination through r-ss in P-72-BVO during water oxidation. This phenomenon resulted in the remarkable η_{trans} of 95 %, promoting the activity of BVO photoanode in PEC water oxidation. Furthermore, NiOOH/FeOOH OEC-decorated P-72-BVO photoanodes showed the superior PEC performance, with an impressive ABPE of 1.4 % at 0.62 V$_{RHE}$ and the remarkable chemical stability maintaining over 90 % of η_f during PEC water splitting. These findings provide a facile and effective method for producing ov$_s$ in semiconductor photoanodes and offer valuable insights into charge carrier dynamics, enabling the enhancement of photoactivity for practical green H$_2$ production in PEC water splitting.

CRediT authorship contribution statement

Kai-An Tsai: Methodology, Investigation, Data curation, Formal analysis, Validation, Writing – original draft. **Chien-Chih Lai:** Methodology, Investigation, Data curation, Formal analysis, Validation. **Yu-Hung Chen:** Methodology, Investigation, Data curation, Formal analysis, Validation, Visualization, Resources. **Ing-Chi Leu:** Investigation, Resources. **Jui-Cheng Chang:** Investigation, Resources. **Che-Yu Kuo:** Data curation, Validation. **Shih-Wen Tseng:** Investigation, Resources. **Yan Li:** Investigation, Resources. **Ying-Chih Pu:** Conceptualization, Writing – review & editing, Supervision, Project administration.

Declaration of Competing Interest

The authors declare that they have no known competing financial interests or personal relationships that could have appeared to influence the work reported in this paper.

Data availability

No data was used for the research described in the article.

Acknowledgement

Appendix A. Supporting information

Supplementary data associated with this article can be found in the online version at doi:10.1016/j.apcatb.2023.123288.

References

[1] Q. Hassan, A.M. Abdulateef, S.A. Hafedh, A. Al-samari, J. Abdulateef, A.Z. Sameen, H.M. Salman, A.K. Al-Jiboory, S. Wieteska, M. Jaszczur, Int. J. Hydrog. Energy 48 (2023) 17383–17408.
[2] M. Isaacs, J. Garcia-Navarro, W.-J. Ong, P. Jiménez-Calvo, Glob. Chall. 7 (2023), 2200165.
[3] Z. Li, S. Fang, H. Sun, R.-J. Chung, X. Fang, J.-H. He, Adv. Energy Mater. 13 (2023), 2203019.
[4] C. Jiang, S.J.A. Moniz, A. Wang, T. Zhang, J. Tang, Chem. Soc. Rev. 46 (2017) 4645–4660.
[5] J.H. Kim, D. Hansora, P. Sharma, J.-W. Jang, J.S. Lee, Chem. Soc. Rev. 48 (2019) 1908–1971.
[6] S. Li, W. Xu, L. Meng, W. Tian, L. Li, Small Sci. 2 (2022), 2100112.
[7] W. Yang, R.R. Prabhakar, J. Tan, S.D. Tilley, J. Moon, Chem. Soc. Rev. 48 (2019) 4979–5015.
[8] Y. Yang, S. Niu, D. Han, T. Liu, G. Wang, Y. Li, Adv. Energy Mater. 7 (2017), 1700555.
[9] C. Liu, N.P. Dasgupta, P. Yang, Chem. Mater. 26 (2014) 415–422.
[10] S. Wang, X. Wang, B. Liu, Z. Guo, K. Ostrikov, L. Wang, W. Huang, Nanoscale 13 (2021) 17989–18009.
[11] M.A. Gaikwad, U.P. Suryawanshi, U.V. Ghorpade, J.S. Jang, M.P. Suryawanshi, J. H. Kim, Small 18 (2022), 2105084.
[12] W. Bai, Y. Zhou, G. Peng, J. Wang, A. Li, P.F.-X. Corvini, Appl. Catal. B Environ. 315 (2022), 121606.
[13] H. Pei, S. Xu, Y. Zhang, Y. Zhou, R. Li, T. Peng, Appl. Catal. B Environ. 318 (2022), 121865.
[14] C.-C. Lai, J.-W. Chen, J.-C. Chang, C.-Y. Kuo, Y.-C. Liu, J.-C. Yang, Y.-T. Hsieh, S.-W. Tseng, Y.-C. Pu, ACS Appl. Mater. Interfaces 14 (2022) 24919–24928.
[15] Z. Xie, D. Chen, J. Zhai, Y. Huang, H. Ji, Appl. Catal. B Environ. 334 (2023), 122865.
[16] B.S. Kalanoor, H. Seo, S.S. Kalanur, Mater. Sci. Energy Technol. 4 (2021) 317–328.
[17] J. Lin, X. Han, S. Liu, Y. Lv, X. Li, Y. Zhao, Y. Li, L. Wang, S. Zhu, Appl. Catal. B Environ. 320 (2023), 121947.
[18] W. Qiu, S. Xiao, J. Ke, Z. Wang, S. Tang, K. Zhang, W. Qian, Y. Huang, D. Huang, Y. Tong, S. Yang, Angew. Chem. Int. Ed. 58 (2019) 19087–19095.
[19] R.-T. Gao, L. Wang, Angew. Chem. Int. Ed. 59 (2020) 23094–23099.
[20] W. Wang, P.J. Strohbeen, D. Lee, C. Zhou, J.K. Kawasaki, K.-S. Choi, M. Liu, G. Galli, Chem. Mater. 32 (2020) 2899–2909.
[21] Z. Tian, P. Zhang, P. Qin, D. Sun, S. Zhang, X. Guo, W. Zhao, D. Zhao, F. Huang, Adv. Energy Mater. 9 (2019), 1901287.
[22] S. Wang, T. He, P. Chen, A. Du, K. Ostrikov, W. Huang, L. Wang, Adv. Mater. 32 (2020), 2001385.
[23] Q. Qin, Q. Cai, J. Li, C. Jian, W. Hong, W. Liu, Sol. RRL 3 (2019), 1900301.
[24] J.-B. Pan, B.-H. Wang, J.-B. Wang, H.-Z. Ding, W. Zhou, X. Liu, J.-R. Zhang, S. Shen, J.-K. Guo, L. Chen, C.-T. Au, L.-L. Jiang, S.-F. Yin, Angew. Chem. Int. Ed. 60 (2021) 1433–1440.
[25] B. Liu, X. Wang, Y. Zhang, L. Xu, T. Wang, X. Xiao, S. Wang, L. Wang, W. Huang, Angew. Chem. Int. Ed. 62 (2023), e202217346.
[26] B. Chen, D. Li, Z. Yang, Q. Li, X. Chen, L. Li, W. Shi, Chem. Eng. Sci. 251 (2022), 117433.
[27] J. Hu, X. Zhao, W. Chen, H. Su, Z. Chen, J. Phys. Chem. C 121 (2017) 18702–18709.
[28] S. Jin, X. Ma, J. Pan, C. Zhu, S.E. Saji, J. Hu, X. Xu, L. Sun, Z. Yin, Appl. Catal. B Environ. 281 (2021), 119477.
[29] Y. Peng, H. Wu, H. Yuan, F.-F. Li, X. Zou, Y.H. Ng, H.-Y. Hsu, Sustain. Energy Fuels 5 (2021) 2284–2293.
[30] K.E. Knowles, M.D. Koch, J.L. Shelton, J. Mater. Chem. C 6 (2018) 11853–11867.
[31] S. Selim, E. Pastor, M. García-Tecedor, M.R. Morris, L. Francàs, M. Sachs, B. Moss, S. Corby, C.A. Mesa, S. Gimenez, A. Kafizas, A.A. Bakulin, J.R. Durrant, J. Am. Chem. Soc. 141 (2019) 18791–18798.
[32] M. Forster, D.W.F. Cheung, A.M. Gardner, A.J. Cowan, J. Chem. Phys. 153 (2020), 150901.
[33] Y.-H. Chen, K.-A. Tsai, T.-W. Liu, Y.-J. Chang, Y.-C. Wei, M.-W. Zheng, S.-H. Liu, M.-Y. Liao, P.-Y. Sie, J.-H. Lin, S.-W. Tseng, Y.-C. Pu, J. Phys. Chem. Lett. 14 (2023) 122–131.
[34] A.-M. Chang, Y.-H. Chen, C.-C. Lai, Y.-C. Pu, ACS Appl. Mater. Interfaces 13 (2021) 5721–5730.
[35] L. Francàs, S. Selim, S. Corby, D. Lee, C.A. Mesa, E. Pastor, K.-S. Choi, J.R. Durrant, Chem. Sci. 12 (2021) 7442–7452.
[36] D.K. Lee, K.-S. Choi, Nat. Energy 3 (2018) 53–60.
[37] H. Duan, H. Wu, H. Zhong, X. Wang, W. Wan, D. Li, G. Cai, C. Jiang, F. Ren, J. Phys. Chem. C 126 (2022) 7688–7695.
[38] M. Morales-Masis, L. Ding, F. Dauzou, Q. Jeangros, A. Hessler-Wyser, S. Nicolay, C. Ballif, APL Mater. 2 (2014), 096113.
[39] Y.-C. Pu, W.-T. Chen, M.-J. Fang, Y.-L. Chen, K.-A. Tsai, W.-H. Lin, Y.-J. Hsu, J. Mater. Chem. A 6 (2018) 17503–17513.
[40] I. Abdellaoui, M.M. Islam, M. Remeika, Y. Higuchi, T. Kawaguchi, T. Harada, C. Budich, T. Maeda, T. Wada, S. Ikeda, T. Sakurai, J. Phys. Chem. C 124 (2020) 3962–3972.
[41] X. Xu, Y. Xu, F. Xu, G. Jiang, J. Jian, H. Yu, E. Zhang, D. Shchukin, S. Kaskel, H. Wang, J. Mater. Chem. A 8 (2020) 1636–1645.
[42] S. Kumar, S. Ahirwar, A.K. Satpati, RSC Adv. 9 (2019) 41368–41382.
[43] D. Kong, J. Qi, D. Liu, X. Zhang, L. Pan, J. Zou, Trans. Tianjin Univ. 25 (2019) 340–347.
[44] J. Cui, M. Daboczi, M. Regue, Y.-C. Chin, K. Pagano, J. Zhang, M.A. Isaacs, G. Kerherve, A. Mornto, J. West, S. Gimenez, J.-S. Kim, S. Eslava, Adv. Funct. Mater. 32 (2022), 2207136.
[45] J.K. Cooper, S.E. Reyes-Lillo, L.H. Hess, C.-M. Jiang, J.B. Neaton, I.D. Sharp, J. Phys. Chem. C 122 (2018) 20642–20652.
[46] D. Chen, Z. Liu, S. Zhang, Appl. Catal. B Environ. 265 (2020), 118580.
[47] Y. Zhang, L. Xu, B. Liu, X. Wang, T. Wang, X. Xiao, S. Wang, W. Huang, ACS Catal. 13 (2023) 5938–5948.